DESIGN, PRODUCTION, AND APPLICATIONS OF STEELS FOR A SUSTAINABLE FUTURE

Effect of Plastic Deformation on the Mechanical Properties of Dual-Phase Steels Using Nanoindentation

DURSUN EKMEKCI,[1] ALTUĞ UŞUN,[2] and ÖMER NECATI CORA ![ORCID][2,3,4]

1.—Department of Mechanical Engineering, Gümüşhane University, 29100 Gümüşhane, Türkiye.
2.—Department of Mechanical Engineering, Karadeniz Technical University, 61080 Trabzon, Türkiye. 3.—e-mail: oncora@ktu.edu.tr. 4.—e-mail: necaticora@gmail.com

The mechanical properties of two advanced high-strength steels (AHSS), DP 1000 and DP 1200 dual-phase (DP) grades, under deformed and undeformed conditions, were investigated using nanoindentation, and the results were compared with those obtained from the conventional methods. To this goal, 3-point bending tests were applied to induce deformation in the samples. Before and after these tests, nanoindentations were performed at different forces and indentation depths. In addition to the hardness and modulus of elasticity values of the steels, the residual stresses on the samples after deformation were obtained by using the equations suggested in the literature, also with x-ray diffraction (XRD). Finite element (FE) modeling of 3-point bending and nanoindentation were performed to obtain stress–strain curves of the materials numerically. The stress–strain curves obtained by numerical analysis agree well with those reported in the literature. The variations of the hardness and modulus of elasticity values are narrower for deeper indentation (50 nm versus 200 nm), and the effect of deformation is more pronounced on the modulus of elasticity values (10–30% increase with the deformation) while hardness values increased with the effect of deformation, 10% at most.

INTRODUCTION

Advanced and ultra-high strength steels (AHSS, UHSS) have been increasingly used in the automotive industry since their first exploitation, and this has led to reduced vehicle weight while maintaining strength and safety (e.g., higher crash energy absorption capacity) and increasing fuel efficiency. Therefore, AHSS is among the most exploited body-in-white (BIW) materials. As an example, AHSS/UHSS utilization in the 2021 Chevrolet Trailblazer increased from 23% to 42% compared to its predecessor.[1] Among the AHSS variants, dual-phase (DP) steels exhibit good hardening properties and therefore are preferred in critical applications including A, B, and C pillars, roof rails, rockers, seat tracks and frames, front side members, roof bows, bumper reinforcements, etc. Its microstructure consists of martensite (provides high strength) and ferrite

matrix phases (provides ductility). The tensile strength of DP steels ranges from 500 to 1200 MPa, and the strength level depends on the amount of martensite in the microstructure, which is usually in the range of 5%–20%[2] yet it can be as high as 86%.[3] There are various conventional and recently developed techniques to analyze and acquire mechanical properties in the literature. Nanoindentation is one of those techniques that researchers are increasingly adopting. Basantia et al.[4] investigated the role of various microstructural parameters on the nanohardness of different phases in ferrite-martensite (FM), ferrite-bainite (FB), and ferrite-pearlite (FP) steels. FM, FB, and FP containing almost the same ferrite amount were subjected to appropriate heat treatment dual-phase microstructures. They characterized the microstructures of DP steels and measured macro-, micro-, and nano-hardness Values and tensile properties. Apart from pearlite, the nanohardness values of the phases forming FM and FB steels were significantly affected by the carbon percentage of the two phases. Meneses-Amador et al.[5] employed nanoindentation

with a Berkovich diamond indenter and a load of 50 mN to acquire the yield stress and Young's modulus of the boride layer formed on the surface of the AISI M2 steel samples. Costin et al. used micro-testing techniques to assess and compare the mechanical properties of acicular ferrite and bainite and tried to understand their effects on the bulk properties of iron alloys.[6] Nanoindentation was applied to evaluate the modulus of elasticity, yield strength, stiffness, and strain-hardening exponent of both micro-substituents. They noted that, on a microscale, acicular ferrite and upper bainite had very similar mechanical properties despite their different microstructures. Li et al. obtained the force–displacement curves of stainless steel (SS 302) and Ti-6Al-4 V α phases by microindentation.[7] Determining the mechanical properties for different phases of materials in microstructure contributed to the understanding of mechanical properties in micro/nano-scale and micromechanical modeling studies. Li et al. used microindentation to study the fracture energy and toughness of the Ti-6A-4 V alloy. They used various maximum indentation force values in the range of 50 – 4900 mN and found that cracks are formed above 4500 mN loading level.[8] In another study, microindentation was used to determine the mechanical properties of compacted and sintered copper powders and a copper substrate.[9] More recently, Ekmekci and Cora used depth-sensing indentation technique to reveal the effects of different indentation load levels (50–300 mN) and types of indentation (e.g., conventional, cyclic, and multi-step) on the mechanical properties of DP 800 steel sample. It was concluded that the load levels employed led to overall material response rather than its constituents.[10]

This study, different from existing literature, aimed to investigate the effect of deformation (hardness, modulus of elasticity, residual stress, and stress–strain curves) on ultra-high strength steels in detail employing nanoindentation along with some complementary techniques. To this goal, the samples were first subjected to 3-point bending tests. Before and after the 3-point bending tests, nanoindentation was performed to reveal the effect of deformation on the mechanical properties. XRD and scanning electron microscopy (SEM) analyses were also carried out on the sample to obtain the residual stresses and investigate the microstructure, respectively. In addition, residual stress values were calculated based on suggested equations in the literature.

EXPERIMENTAL

Materials

The mechanical and chemical properties of dual-phase automotive steels used in this study are given in Table I. DP 1000 and DP 1200 automotive steel sheet blanks used in this study were supplied by Sweden-based steel manufacturer SSAB. These steels exhibit ultra-high-strength and formability performance and are preferred in autobody components.

The surfaces of the samples were prepared using 320, 600, 1000, 1200, 1500, and 2000 grit SiC sandpaper, respectively. Later, a fine polishing was applied to the sample surfaces with 1-μm diamond and 0.06-μm alumina suspensions. For image analysis, the samples were etched in Nital (5% HNO_3 and 95% ethanol) solution for 5 s. Figure 1 shows the microstructural images of DP 1000 and DP 1200 samples obtained by an FEI-Quanta 250 SEM (FEI Company, Hillsboro, OR, USA) upon etching. It was determined using ImageJ software (National Institutes of Health, Bethesda, MD, USA) that DP 1000 has 40.6% ferrite + 59.4% martensite while DP 1200 has 36.6% ferrite + 63.4% martensite.

Three-Point Bending Tests and FEA

To induce deformation in the automotive steel samples, 3-point bending tests were employed. Figure 2 shows 3-point bending test sample dimensions (Fig. 2a), deformed sample, and extracted parts using abrasive water-jet cutting for nanoindentation analysis (Fig. 2b), and the FE model was established. The 3-point bending tests were performed using an Instron-3382 electro-mechanic test frame (Instron Inc., Norwood, MA, USA) per ASTM D790 standard, and punch movement speed was set as 0.05 mm/s in the vertical direction. After the 3-point bending test, nanoindentation, residual stress from XRD, micro-Vickers measurements, atomic force microscope (AFM), and SEM analysis were performed on the deformed and undeformed zones of the samples. The 3-point bending test was modeled and analyzed with the commercially available FE package ASNYS 19 (Fig. 2c) to investigate the stress and strain values. The model consisted of 12,294 rectangular 4-node square elements with 0.57-mm edge length. The plastic behavior of the material was represented by the von Mises yield criterion, and the material was assumed to be isotropic. All the nodes of the model are fixed against rotation around the x- and z-axes (Fig. 2c).

Nanoindentation and Its FEA

A maximum-displacement controlled nanoindentation was performed using TI 950 TriboIndenter (Bruker Inc., Billerica, MA, USA) with a sharp triangular pyramid Berkovich indenter. A 5 × 5 indentation matrix was applied to the sample surfaces with two different maximum indentation depth values, namely, 50 nm and 200 nm. The indentation imprints were scrutinized with in situ SPM imaging available within TI 950 TriboIndenter to reveal a possible pile-up effect.

Nanoindentation measurements are standardized with ASTM E2546 and ISO 14577. The reduced

Table I. Chemical composition and mechanical properties of dual-phase steels[11,12]

Steels	Yield strength (MPa)	Tensile strength (MPa)	C%	Si%	Mn%	P%	S%	Al%	Nb%
DP 1000	700–950	1000–1200	0.15	0.5	1.5	0.015	0.002	0.04	0.015
DP 1200	950–1250	1200–1400	0.17	0.5	1.6	0.015	0.002	0.04	0.015
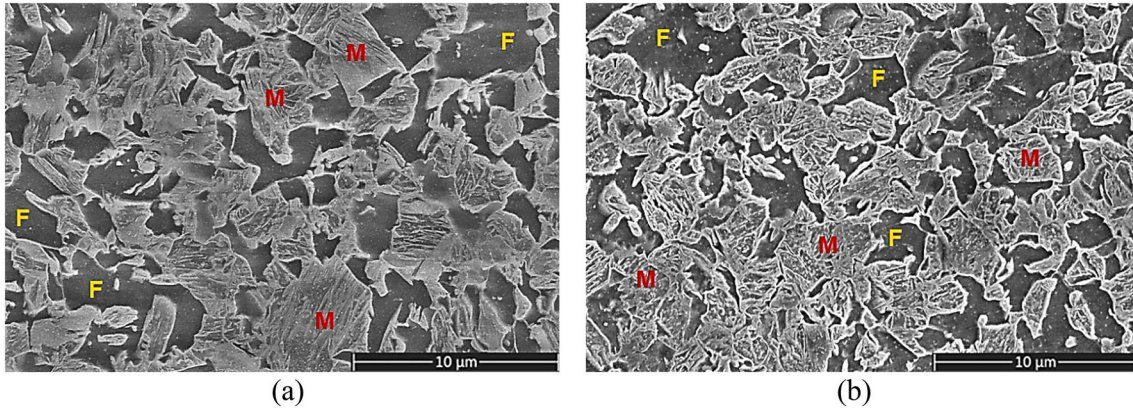
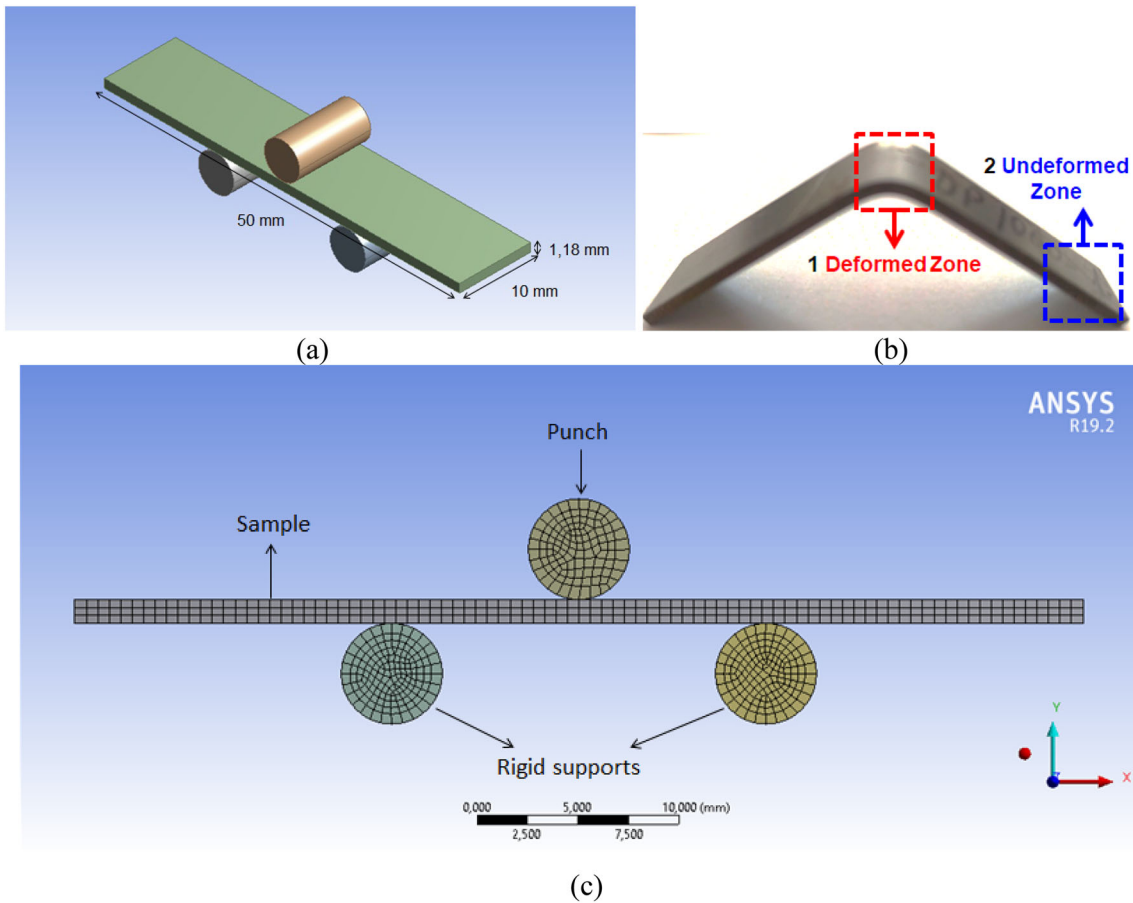Fig. 1. SEM images of (a) DP 1000 and (b) DP 1200 samples (F: ferrite, M: martensite).

Fig. 2. (a) Dimensions of DP steel sheet sample, (b) sample extraction from undeformed and deformed zones for analysis after the 3-point bending test, (c) FE model of 3-point bending test.

modulus of elasticity is calculated from the contact stiffness (S) and the nanoindentation projected area (A) in Eq. 1. After the reduced modulus of elasticity (E_r) is found, it is substituted in Eq. 1. The Poisson ratios of the material and the indenter can be calculated by Eq. 2 if the elasticity modulus of the indenter is known.[13,14]

$$S = \frac{dP}{dh}, E_r = \frac{1}{\beta}\frac{\sqrt{\pi}}{2}\frac{S}{\sqrt{A(h_c)}} \quad (1)$$

E_r is the reduced modulus of elasticity, $A(h_c)$ is the projected surface area of the indenter at depth h_c, and β is a geometric constant.

$$\frac{1}{E_r} = \frac{1 - v_{\text{indenter}}^2}{E_{\text{indenter}}} + \frac{1 - v_{\text{material}}^2}{E_{\text{material}}}, \quad (2)$$

$$H = \frac{P_{\max}}{A} \quad (3)$$

E_{indenter} and v_{indenter} are the modulus of elasticity and Poisson ratio of the indenter material, which is diamond (E_{indenter} = 1140 GPa, v_{indenter} = 0.07) in this case. E_{material} and v_{material} are the modulus of elasticity and Poisson ratio of the test material. The hardness of the material is calculated by Eq. 2 where P is the maximum force and A is the projected surface area of the indenter on the material in this equation. Typical force–displacement curves obtained from the depth-controlled nanoindentation test on the DP 1000 sample are given in Fig. 3.

The effect of different maximum indentation depth values on the results was analyzed through one-way ANOVA. According to the one-way ANOVA analysis ($p \leq 0.05$), the changes in both the modulus of elasticity and hardness values for the different depth levels tested were insignificant in relation to the peak force.

Inverse numerical analysis of nanoindentation is widely applied to determine the stress–strain curves of the materials. In the inverse analysis of nanoindentation, the force–displacement response is available yet the material properties are unknown. Therefore, an optimization method should be utilized to determine the mechanical properties of the material of interest. The finite element model established using FE package Ls-Dyna (LSTC, Livermore, CA, USA) is given in Fig. 4. Inverse nanoindentation optimization requires plenty of analysis; therefore, reducing the solution time is important. An axisymmetric model was prepared to reduce the analysis time. Although the three-sided pyramid Berkovich indenter is commonly used in nanoindentation measurements, the equivalent conical indenter approach, whose accuracy has been shown by different researchers,[15,16] was preferred in the numerical analysis. The Berkovich indenter used in the nanoindentation was transformed into a conical shape with a
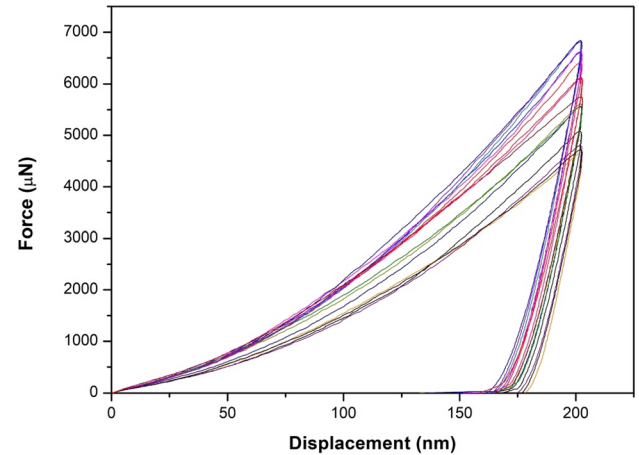

Fig. 3. Force–displacement curves obtained from the nanoindentation applied to the DP 1000 sample.

half apex angle of 70.3° for the two-dimensional axisymmetric model. The indenter was modeled as rigid, and displacement function was defined to the indenter. The bottom and right sides of the sample were fixed. The sample was assumed to be isotropic, and the von Mises yield criterion defined the plastic behavior of the material. Rectangular 4-node shell elements were used to obtain the mesh structure for both the indenter and specimen. Upon mesh convergence optimization, the specimen consisted of 11,967 shell elements. This established two-dimensional axisymmetric finite element model was also used to obtain the stress–strain curve for DP 1000 and DP 1200 steels after nanoindentation testing.

XRD and Nanoindentation-based Residual Stress Measurements

XRD analysis was performed using Explorer (GNR srl, Novara, Italy) to acquire residual stress values on the deformed and undeformed zones of the samples. $\text{Sin}^2\psi$ method was used with an incident angle of $\omega = 3°$, which is the angle between an incident ray on the surface and the normal of the surface at the incidence point. The detailed measurement procedure can be found in the literature.[17,18] Residual stress from XRD was obtained for both materials at a depth of 1.13 μm. Residual stress information can also be obtained using the force–displacement curves obtained from nanoindentation. The nanoindentantion-based residual stress is obtained upon calculating the difference between contact areas and indentation depth of undeformed and deformed parts utilizing indentation force–displacement (P–h) data.[19] Wang et al. calculated the residual stresses with the Eq. 3 using the P_1 and P_2 loads obtained from the nanoindentation, residual depth, h_r, and geometric correction factor $\alpha = 65.3°$.[20]
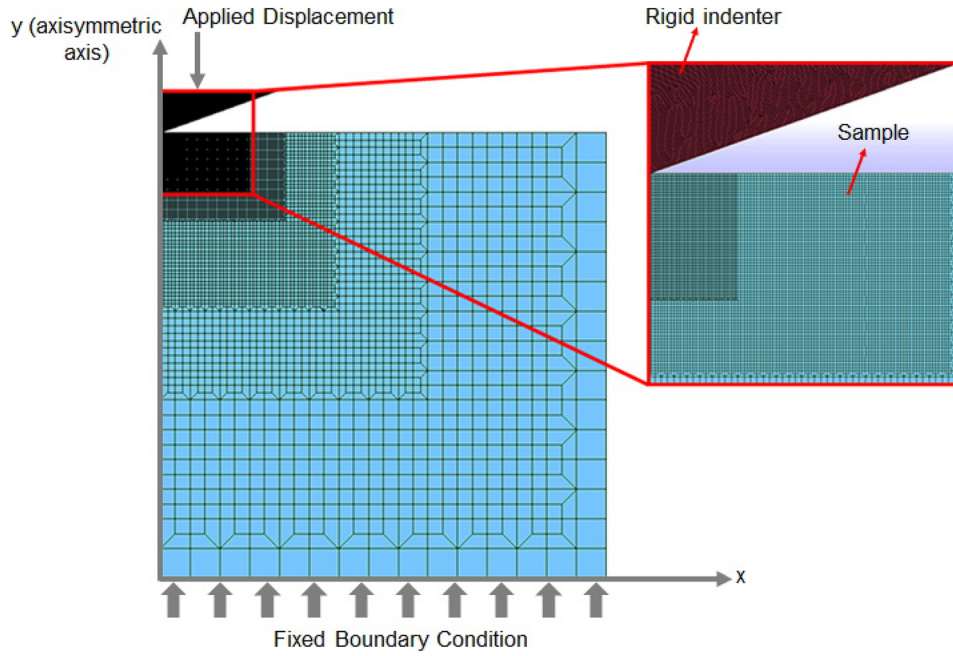
Fig. 4. Two-dimensional axisymmetric finite element model of nanoindentation.
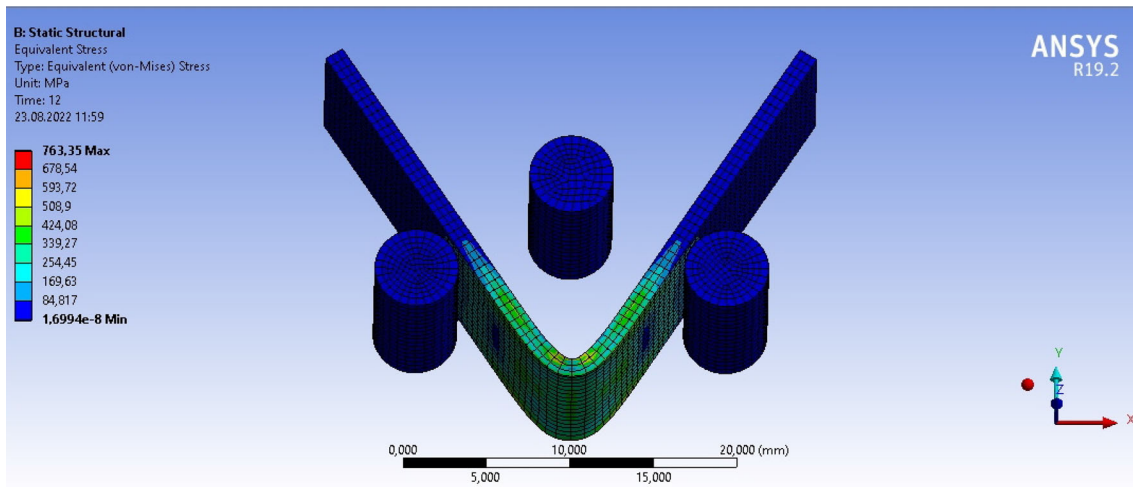

Fig. 5. von Mises equivalent stress distribution on the DP 1000 sample.

$$\sigma_r = \frac{P_1 - P_2}{2\pi \tan^2 \alpha h_r^2} \quad (4)$$

RESULTS AND DISCUSSION

Three-Point Bending Test Results

Considering the sample dimensions, a displacement of approximately 11 mm in the y-direction was applied to the midpoint of the model in the 3-point bending test. This was also performed in the finite element analysis. Figure 5 shows the von Mises equivalent stress distribution obtained by FEA for

the DP 1000 sample. The maximum stress level obtained from the FEA surpassed the yield point of the material, as expected.

Nanoindentation Results

Maximum depth-controlled nanoindentations were carried out to obtain the properties of the materials. Figure 6 shows the hardness and modulus of elasticity values obtained for DP 1000 and DP 1200 samples at maximum indentation depths of 50 and 200 nm. The 5 × 5 matrix nanoindentations were applied to both samples. The maximum force values obtained at these two different maximum depths were 0.9 mN for 50 nm and 7 mN for
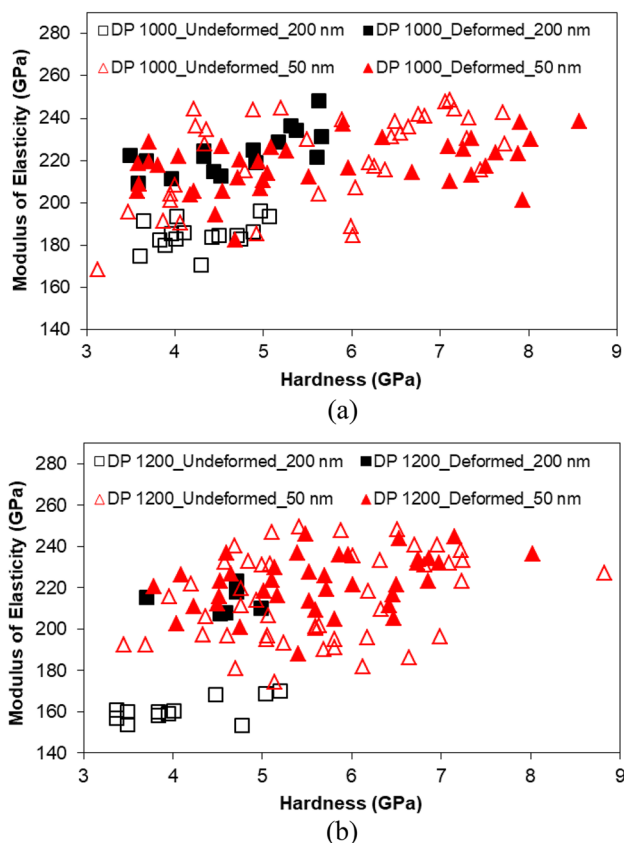
(a)

(b)

Fig. 6. Hardness and modulus of elasticity values obtained with maximum depth control type of nanoindentation (a) for DP 1000 at 50 nm and 200 nm; (b) for DP 1200 at 50 nm and 200 nm.

Table II. Hardness values of ferrite and martensite phases of DP steels reported in the literature

Study by	Material	Hardness (GPa)	
		Ferrite	**Martensite**
Taylor et al.[22]	DP 980	2–3	5–9.5
Rahimi et al.[23]	DP 1180	3.5 − 5.5	6–8.5
Zhang et al.[24]	DP 980	4.05	8.43
Hernandez et al.[25]	DP 980	2–4	6–8
Delince´ et al.[26]	DP 1000	2–4	4–8
Basu et al.[27]	DP 600	2–4	5–9

200 nm. As the materials of interest in this study have two distinct phases, namely ferrite and martensite, and the aim was to reveal the properties of these individual phases. To this goal, samples were etched upon nanoindentation using different methods described in the literature. However, nanoindentation traces after etching could not be detected in SEM. It is thought that the etching eliminated the traces caused by nanoindentation. To prevent this, the etching time should be kept short, or the indentation depth should be increased. Nevertheless, if the etching period is kept short, the etching might not be sufficient to distinguish the phases of the microstructure. If the indentation depth is increased, on the other hand, transition to microindentation so the penetration of the indenter to more than one phase can be possible. The average hardness values for DP 1000 at 50 nm were obtained as 4.93 GPa and 4.36 GPa for undeformed and deformed conditions, respectively. On the other hand, the average hardness values for DP 1200 at 50 nm were recorded as 5.28 GPa and 5.39 GPa, respectively. Hardness values at 200 nm indentation depth were noted for DP 1000 as 4.29 GPa and 4.68 GPa for undeformed and deformed conditions, respectively. For DP 1200, at the same indentation depth (200 nm), the average hardness values were acquired as 4.07 and 4.54 GPa for undeformed and

deformed conditions, respectively. These results show that with the increasing indentation depth (from 50 to 200 nm), the average hardness value of the investigated materials decreased while it increased with deformation in general. In terms of modulus of elasticity, the values tend to increase with deformation and increased indentation depth. For example, average modulus of elasticity values of 201 GPa and 211.9 GPa were recorded for DP 1000 sample at 50 nm depth and undeformed and deformed conditions. On the other hand, average modulus of elasticity values of 185 GPa and 223.8 GPa were recorded again for DP 1000 samples at 200 nm indentation depth for undeformed and deformed conditions, respectively. Notably, the undeformed and deformed measurements could not be obtained from the same point as the nanoindentation itself induces plastic deformation on the surface.

The results obtained at a maximum depth of 50 nm and 200 nm for both materials examined showed that hardness values at 50 nm are considerably more scattered for both materials while relatively narrow variations were observed for the hardness values obtained at 200 nm. This is assumed to have resulted from the fact that the higher the indentation depth, the larger the contact area, and so the overall response of the microstructure rather than the individual phases (ferrite or martensite). For example, in 50-nm measurements, hardness values up to 9 GPa were obtained, which is a sign of martensite phase, while 200 nm measurements yielded hardness values < 6 GPa for both materials. Regarding modulus of elasticity values, the effect of deformation (undeformed vs. deformed) is visible when the measurements at 200 nm are considered. For both materials, the modulus of elasticity values increased with the deformation. Nevertheless, no such trend was observed for the measurements obtained at 50 nm.

It was reported that the hardness of the ferrite and martensite phases in a DP steel depends on many factors including chemical composition, size, morphology, and distribution of phase, apart from the dislocation density and internal stresses.[21] The
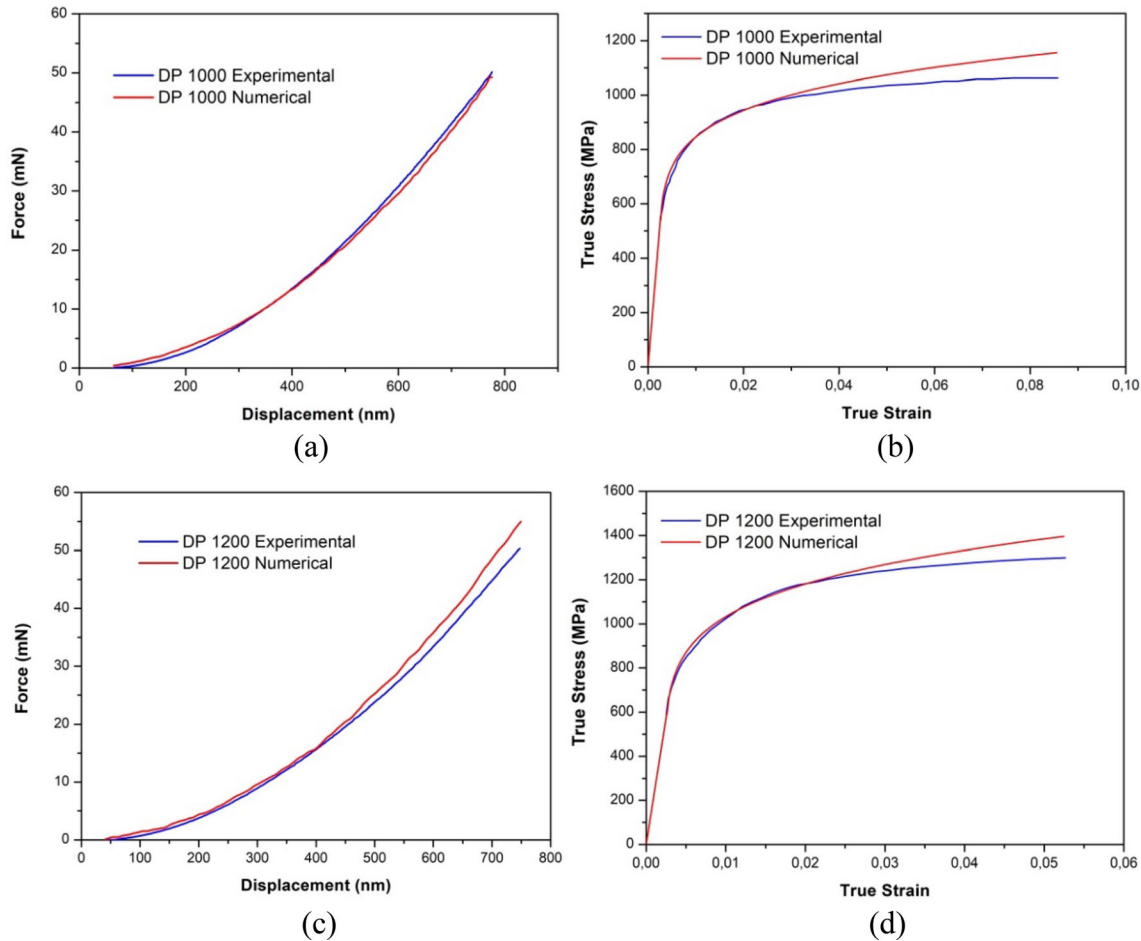
Fig. 7. Comparison of experimentally and numerically obtained (a) force–displacement curves, (b) stress–strain curves for DP 1000, (c) force–displacement curves, and (d) stress–strain curves for DP 1200.

literature data given in Table II indicate that relatively low hardness values correspond to ferrite and high-hardness values to martensite. The hardness value variation for the DP 1000 and DP 1200 microstructures was obtained between approximately ∼ 4 GPa (mainly ferrite) and ∼ 9 GPa (mainly martensite) in the current study. These findings led to the conclusion that the measurements at 50 nm yielded hardness values of individual phases in the microstructure while the measurements at 200 nm demonstrated the resultant hardness value of the microstructure rather those for microconstituents.

Results of FEA of Nanoindentation

In addition to the acquisition of basic mechanical properties, finite element models were established to obtain stress–strain curves of the materials. The inverse finite element method was first proposed by Bucaille et al. to obtain the hardness and elasticity modulus.[28] Later, this method was widely used to characterize the mechanical behavior of materials. Bouzakis et al. obtained the stress–strain curves from nanoindentation tests performed at various indentation depths.[29] In general, the inverse finite element method is based on systematic changing of the mechanical properties of the material in the finite element model by trial–error method and approximating the real nano- or microindentation curves.[30,31] In other words, this method is based on the minimization of the difference between real and numerical nanoindentation curves. In contrast, the finite element method usually starts with the choice of a formula that can define the stress–strain curve. For example, the commonly used modified Holloman equation to characterize the plastic behavior of materials Eq. 4 is given below:

$$\text{Modified Holloman equation}: \sigma = E^m \sigma_y^{(1-m)} \varepsilon^m \quad (5)$$

where E is Young's modulus, σ is stress, ε strain, σ_y is the yield stress, and m is the hardening exponent. The values of σ_y and m which provides the minimum difference between experimental and numerical curves, are accepted as the mechanical behavior of the material. Within the scope of this study, optimizations were carried out with Ls-Opt using the genetic algorithm method. In optimization, although the number of unknown parameters is

Table III. Comparison of hardening coefficient (m) obtained from current study vs. literature

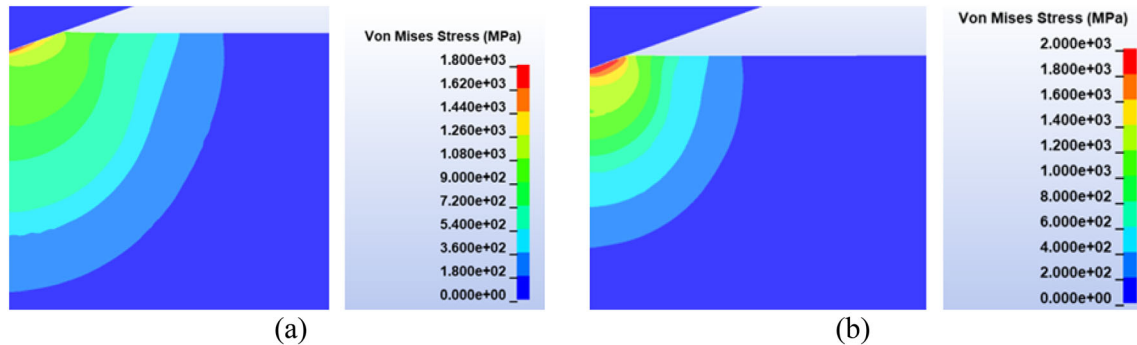| Material	Yield strength, σ_y (MPa)	Hardening coefficient, m (current study)	Hardening coefficient, m (literature)	Difference %
DP 1000	770	0.13	0.12[36]	8.3
DP 1200	950	0.16	0.14[37]	14.3

Fig. 8. von Mises equivalent stress variation from FEA of nanoindentation analysis for (a) DP 1000 and (b) DP 1200 steels.

less than in the other equations, the modified Holloman law Eq. 4, which was reported to provide excellent convergence, was used.[32,33] The inverse finite element method was applied to the nanoindentation of the DP 1000 and DP 1200 samples taken from the deformed region upon 3-point bending test. Experimentally (from the manufacturer of the steels) and numerically obtained (through FEA of nanoindentation) stress–strain curves of dual-phase steels are shown in Fig. 7. As the figures show, numerically obtained stress–strain curves for DP 1000 and DP 1200 steels exhibited good agreement with the experimentally obtained ones by the manufacturer. Even though some divergence occurs in the deformation hardening zone of the DP 1000 and DP 1200 samples, these results show the reliability of the developed model. Material parameters obtained from inverse finite element analysis of nanoindentation are summarized in Table III. These data were found to be in agreement with the yield stress and strain hardening coefficients reported for dual-phase steels.[34,35] Figure 8 shows the equivalent von Mises equivalent stress distribution from nanoindentation of dual-phase steels obtained from FEA.

Comparison of Residual Stresses from XRD Versus Nanoindentation

Residual stresses from XRD measurements on the undeformed and deformed regions of DP 1000 and DP 1200 automotive steel samples were obtained. Measurements were based on 2θ-$\sin^2\psi$ method. The peaks of DP 1000 and DP 1200 samples at 2θ intervals were obtained at angles $2\theta_{110} = 52.379°$, $2\theta_{200} = 77.237°$, and $2\theta_{211} = 99.708°$. Residual

stress values obtained from XRD for the undeformed and deformed DP 1000 samples were + 12 MPa (tensile) and -310 MPa, respectively. On the other hand, higher residual stresses were obtained for DP 1200 samples as − 36 MPa and − 794 MPa for undeformed and deformed samples, respectively. Notably, deformed samples attained compressive stresses. This can be explained by the deformation mechanism during the 3-point bending test. The samples were subjected to tensile stress due to bending and then springback (as in Fig. 5), which causes compressive stress on the outer surface of the bent sample. In the DP 1000 sample, however, deformation of the samples caused diminishing of the compressive stress effect and yielded positive residual stress of 12 MPa.

Nanoindentation-based residual stresses, on the other hand, were calculated using P_1, P_2, and h_r values as given in Eq. 3. The residual stresses from nanoindentation for DP 1000 and DP 1200 materials at deformed conditions were obtained as − 398 MPa and − 885 MPa, respectively. Comparison with the residual stress values obtained from XRD showed that the difference is 28% for the DP 1000 sample and 11% for the DP 1200 sample. Zhu et al. noted that the difference between XRD and nanoindentation-based residual stress values may result from 'pile-up' or 'sink-in' deformation around the indentation zone and roughness of the sample surface.[38]

AFM Analysis

Images of indents on the samples were obtained with the AFM available in the nanoindenter. Figure 9 shows the AFM images of the 3 × 3 matrix
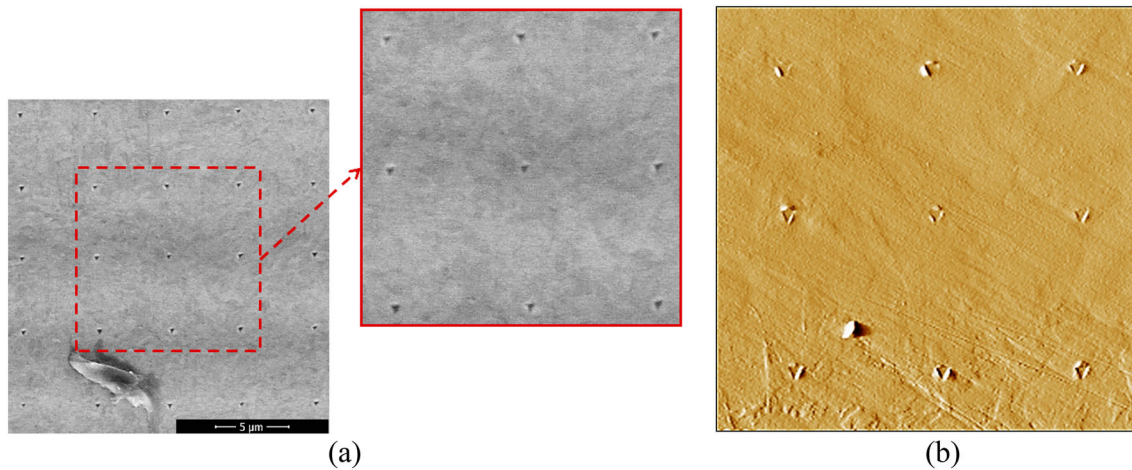
Fig. 9. (a) The region where AFM analysis is performed over the nanoindentation area in automotive steel samples (3 × 3 measurement area), (b) AFM image of DP 1200 steel.

indentation part of a 5 × 5 matrix measurement. The average roughness values of the polished sample surfaces were obtained between 0.21–0.35 μm. The surface roughness of the DP 1200 sample was slightly higher than the surface roughness of the DP 1000 sample.

Pile-up Analysis

During the indentation, plastically deformed material tends to flow up against the faces of the indenter and is pushed away from the center of the indent. This phenomenon is known as "pile-up," and it affects the calculated contact area and consequently the reliability of the mechanical properties. h_f/h_{max} values (h_f is the final indentation depth, and h_{max} is the maximum indentation depth) were calculated to reveal the possible pile-up effect. It is noted in the literature that pile-up is significant if h_f/h_{max} is close to 1 and the work-hardening is small. If $h_f/h_{max} < 0.7$, on the other hand, none or only a very small pile-up is observed regardless of whether the material work-hardened or not.[14] The average value of h_f/h_{max} was calculated as 0.78 for DP 1000 and 0.75 for DP 1200. Therefore, it was concluded that the pile-up is not at a significant level.

CONCLUSION

This study aimed to use nanoindentation as an alternative method to determine the mechanical properties of materials. In this context, first, nanoindentations were performed on the automotive sheet samples to obtain mechanical properties. Within the limitations of the study, the main outcomes are as follows:

– The variation in the mechanical properties was found to be smaller with increasing indentation depth from 50 to 200 nm. This can be attributed to the acquisition of mechanical properties of the

individual phases (ferrite, martensite) at 50 nm while the overall material response was obtained at 200 nm because of the increased size of the indent leading to indentation on multiple phases concurrently.
– The effect of deformation was more pronounced on the modulus of elasticity values. With the deformation, it was observed that both hardness and modulus of elasticity values increase. The increase for both hardness and modulus of elasticity values was higher in 200 nm maximum indentation depth measurement.
– Nanoindentation technique has been used to acquire the residual stresses of automotive steel samples. It was noted that the residual stresses obtained through the nanoindentation-based calculation method can be used with caution as changing levels of 11–28% discrepancy are available.
– The finite element model of the nanoindentation was established, and the force–displacement curve obtained from the nanoindentation was used as an input in the finite element analysis. The model was validated by the high overlap of the force–displacement curves obtained from the FEA with the experimental data obtained from the indentation. Furthermore, it was observed that the stress–strain curves given by the manufacturer of DP 1000 and DP 1200 automotive steels had a high degree (90%) of agreement with the curves obtained by numerical analysis till the end of the deformation hardening zone.

CONFLICT OF INTEREST

The authors declare that they have no conflict of interest.

REFERENCES

1. Y. Kim, Great Designs in Steel Seminar, (2021), https://www.steel.org/gdis-2021-_-track-1_02_kim_chevrolet-trailblazer/. Accessed 2 Sep 2022.
2. T. Ishikawa, Ch.1 in Microstructure Evolution in Metal Forming Processes (Eds. Jianguo Lin, Daniel Balint, Maciej Pietrzyk, Woodhead Publishing. https://doi.org/10.1533/9780857096340.1.3. (2012).
3. S.K. Paul, N. Stanford, and T. Hilditch, *Mater Sci. Eng. A* 638, 296 https://doi.org/10.1016/j.msea.2015.04.059 (2015).
4. S. Majumdar, S. Roy, and K.K. Ray, *Fatigue Fract Eng. Mater. Struct.* 40, 315 https://doi.org/10.1111/ffe.12491 (2017).
5. S.K. Basantia, A. Bhattacharya, N. Khutia, and D. Das, *Mater. Today Commun.* 30, 103125 https://doi.org/10.1016/j.mtcomm.2022.103125 (2022).
6. A. Meneses-Amador, D. Blancas-Pérez, R. Corpus-Mejía, G.A. Rodríguez-Castro, J. Martínez-Trinidad, and L.F. Jiménez-Tinoco, *J. Mater. Eng. Perform.* 27, 2089 https://doi.org/10.1007/s11665-018-3150-z (2018).
7. W.L. Costin, O. Lavigne, and A. Kotousov, Mater. *Sci. Eng. A* 663, 193 https://doi.org/10.1016/j.msea.2016.03.103 (2016).
8. J. Li, F. Li, X. Ma, Q. Wang, J. Dong, and Z. Yuan, *Mater Des.* 67, 623 https://doi.org/10.1016/j.matdes.2014.11.010 (2015).
9. D. Ekmekci, F. Yılmaz, U. Kölemen, and Ö.N. Cora, *Appl. Phys. A* 123, 705 https://doi.org/10.1007/s00339-017-1327-1 (2017).
10. D. Ekmekci, and Ö. N, *Cora. Appl. Phys. A* 126, 916 https://doi.org/10.1007/s00339-020-04095-z (2020).
11. SSAB Tunnplat Docol® 1000 DP High-strength Steel, https://www.matweb.com/search/datasheet.aspx?matguid=def3d5be3ce1447c8af45a4cafe6ec43. Accessed 13 Feb 2023.
12. SSAB Tunnplat Docol® 1200 DP High-strength Steel, https://www.matweb.com/search/datasheet.aspx?matguid=082094564da84b9dbb990ad8817a0989. Accessed 13 Feb 2023.
13. A.C. Fischer-Cripps, *Surf. Coat. Technol.* 200, 4153 https://doi.org/10.1016/j.surfcoat.2005.03.018 (2006).
14. W.C. Oliver, and G.M. Pharr, *J. Mater. Res.* 19, 3 https://doi.org/10.1557/jmr.2004.19.1.3 (2004).
15. M. Lichinchi, C. Lenardi, J. Haupt, and R. Vitali, *Thin Solid Films* 312, 240 https://doi.org/10.1016/S0040-6090(97)00739-6 (1998).
16. K.D. Bouzakis, M. Pappa, G. Maliaris, and N. Michailidis, *Surf. Coat. Technol.* 215, 218 https://doi.org/10.1016/j.surfcoat.2012.09.061 (2013).
17. B.D. Cullity and S.R. Stock, Elements of X-ray Diffraction, Pearson Education Limited Third Edition 451–487 (2014).
18. P.J. Withers, and H. Bhadeshia, Mater. *Sci. Technol.* 17, 355 https://doi.org/10.1179/026708301101509980 (2001).
19. A.E. Giannakopoulos, and S. Suresh, *Scr. Mater.* 40, 1191 https://doi.org/10.1016/S1359-6462(99)00011-1 (1999).
20. Q. Wang, K. Ozaki, H. Ishikawa, S. Nakano, and H. Ogiso, *Nucl. Instrum. Methods Phys. Res. B* 242, 88 https://doi.org/10.1016/j.nimb.2005.08.008 (2006).
21. A. Kumar, S.B. Singh, and K.K. Ray, *Mater Sci. Eng. A* 474, 270 https://doi.org/10.1016/j.msea.2007.05.007 (2008).
22. M.D. Taylor, E. De Moor, J.G. Speer, and D.K. Matlock, *Steel Res Int.* 92, 2100281 https://doi.org/10.1002/srin.202100281 (2021).
23. R.M. Rahimi, and D.F. Bahr, *Mater Sci. Eng. A* 756, 328 https://doi.org/10.1016/j.msea.2019.04.063 (2019).
24. F. Zhang, A. Ruimi, P.C. Wo, and D.P. Field, *Mater Sci. Eng. A* 659, 93 https://doi.org/10.1016/j.msea.2016.02.048 (2016).
25. V.H.B. Hernandez, S.K. Panda, Y. Okita, and N.Y. Zhou, *J. Mater. Sci.* 45, 1638 https://doi.org/10.1007/s10853-009-4141-0 (2010).
26. M. Delince, P.J. Jacques, and T. Pardoen, *Acta Mater.* 54, 3395 https://doi.org/10.1016/j.actamat.2006.03.031 (2006).
27. S. Basu, N.G. Mathews, T.S. Chaudharı, and B.N. Jaya, *Jom* 74, 2245 https://doi.org/10.1007/s11837-022-05298-w (2022).
28. J.L. Bucaille, S. Stauss, E. Felder, and J. Michler, *Acta Mater.* 51, 1663 https://doi.org/10.1016/S1359-6454(02)00568-2 (2003).
29. K.D. Bouzakis, and N. Michailidis, *Mater Charact.* 56, 147 https://doi.org/10.1016/j.matchar.2005.10.005 (2006).
30. K.H. Chung, W. Lee, J.H. Kim, C. Kim, S.H. Park, D. Kwon, and K. Chung, *Int. J. Solids Struct.* 46, 344 https://doi.org/10.1016/j.ijsolstr.2008.08.041 (2009).
31. J. Lee, C. Lee, and B. Kim, Mater. *Des.* 30, 3395 https://doi.org/10.1016/j.matdes.2009.03.030 (2009).
32. D.M. De Bono, T. London, M. Baker, and M.J. Whiting, *Int. J. Mech. Sci.* 123, 162 https://doi.org/10.1016/j.ijmecsci.2017.02.006 (2017).
33. C. Moussa, O. Bartier, G. Mauvoisin, P. Pilvin, and G. Delattre, *J. Mater. Res.* 27, 20 https://doi.org/10.1557/jmr.2011.303 (2012).
34. T.T. Huang, R.B. Gou, W.J. Dan, and W.G. Zhang, *Mater Sci. Eng. A* 672, 88 https://doi.org/10.1016/j.msea.2016.06.066 (2016).
35. M. Gaško, and G. Rosenberg, *Mater Eng.* 18, 155 (2011).
36. A. Saai, O.S. Hopperstad, Y. Granbom, and O.G. Lademo, *Procedia Mater Sci.* 3, 900 https://doi.org/10.1016/j.mspro.2014.06.146 (2014).
37. C.M. Poulin, Y.P. Korkolis, B.L. Kinsey, and M. Knezevic, *Mater Des.* 161, 95 https://doi.org/10.1016/j.matdes.2018.11.022 (2019).
38. L. Zhu, B. Xu, H. Wang, and C. Wang, *Mater Sci. Eng. A* 536, 98 https://doi.org/10.1016/j.msea.2011.12.078 (2012).